

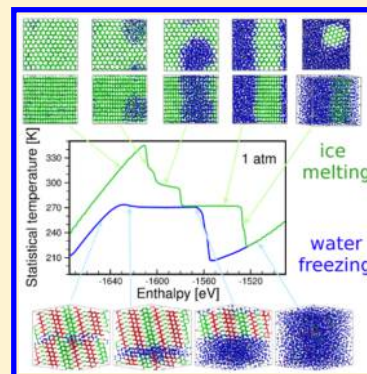
Water Freezing and Ice Melting

Edyta Małolepsza and Tom Keyes*

Department of Chemistry, Boston University, Boston, Massachusetts 02215-2521, United States

S Supporting Information

ABSTRACT: The generalized replica exchange method (gREM) is designed to sample states with coexisting phases and thereby to describe strong first order phase transitions. The isobaric MD version of the gREM is presented and applied to the freezing of liquid water and the melting of hexagonal and cubic ice. It is confirmed that coexisting states are well-sampled. The statistical temperature as a function of enthalpy, $T_S(H)$, is obtained. Hysteresis between freezing and melting is observed and discussed. The entropic analysis of phase transitions is applied and equilibrium transition temperatures, latent heats, and surface tensions are obtained for hexagonal ice \leftrightarrow liquid and cubic ice \leftrightarrow liquid with excellent agreement with published values. A new method is given to assign water molecules among various symmetry types. Pathways for water freezing, ultimately leading to hexagonal ice, are found to contain intermediate layered structures built from hexagonal and cubic ice.



INTRODUCTION

What are the pathways of water freezing or ice melting? This question has not been definitively answered by computer simulations and remains under active investigation because the liquid \leftrightarrow solid transition is first order with a symmetry change and a high free energy barrier. Using standard algorithms with temperature as the control variable, substantial supercooling or superheating is required to drive the transition, leading immediately to ice at $T < T_{eq}$ or liquid at $T > T_{eq}$, respectively, where T_{eq} is the equilibrium transition temperature. Thus, the atomistic pathways for $T \approx T_{eq}$ are obscured.¹

A related question is whether the process of water freezing is in any way different from the reverse process of ice melting. Although ice most often melts at a surface and water freezes at a nucleation site, here we consider pathways connecting pure water and a solid block of ice.

In thermodynamics, freezing and melting are reversible to each other at T_{eq} . As such, a movie of a melting ice block watched from the end to the beginning should be the same as a movie of water freezing.

Although thermodynamics is always correct at the macroscopic level, what if we look at the atomic level in silico?

The difficulties are usefully discussed in terms of the dependence of the entropy, S , upon the potential energy, U (isochoric conditions) or enthalpy, $H = U + pV$ (isobaric conditions, p is pressure, V is volume). Here, we focus on constant pressure. First order transitions are characterized by existence of an energy or enthalpy region where the curvature of the entropy changes from concave to convex ("convex intruder"), whereas the statistical temperature, $T_S(H) = 1/(dS/dH)$, exhibits an S-loop (backbending, see the black/blue line in Figure 1).

As a result, in isothermal simulations at T near T_{eq} (shown as a magenta horizontal line in Figure 1), the equation that is

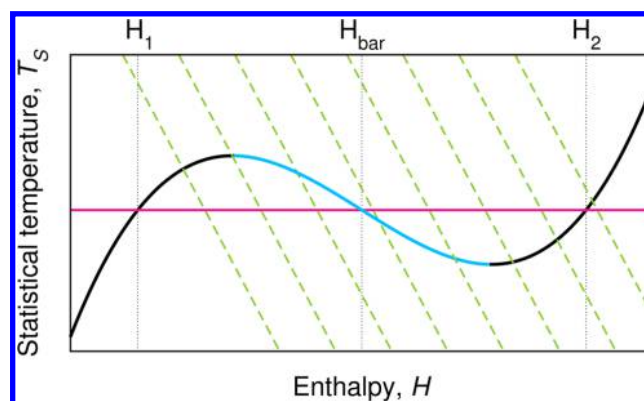


Figure 1. Constant temperature line (magenta) at the transition intersects the S-loop in the statistical temperature three times at H_1 (lower- H homogeneous phase), H_{bar} (barrier), and H_2 (upper- H homogeneous phase). Blue line represents region of coexisting states with strong surface effects in a simulation (the case at hand) or unstable states in a van der Waals model. Examples of generalized temperature $T_\alpha(H)$, see eq 1, are shown as green dashed lines.

solved for the extrema of the enthalpy distribution with a given constant T and function $T_S(H)$, $T = T_S(H^*)$, has three solutions, two free energy minima (maxima of enthalpy distribution) in the pure phases at H_1 and H_2 and a barrier (minimum of enthalpy distribution) at H_{bar} , corresponding to the three intersections of the horizontal constant temperature line with $T_S(H)$.

Consequently, the enthalpy distributions are double peaked around the pure phases at H_1 and H_2 . The simulation is stuck in one or the other while the states along the transition

Received: July 3, 2015

Published: October 12, 2015

pathway between the extrema of T_S , with coexisting phases, are difficult or impossible to sample with $T \approx T_{eq}$. For pure water, this corresponds to the well-known fact that freezing in the lab or in simulation requires deep supercooling.

A solution to this problem was proposed by Kim et al.² as an enhanced sampling algorithm based on a generalized ensemble in combination with replica exchange. The generalized replica exchange method (gREM) uses an enthalpy- (or energy)-dependent generalized temperature, $T_\alpha(H)$, in replica α , such that

$$T_\alpha(H) = \lambda_\alpha + \eta_\alpha(H - H_0) \quad (1)$$

where slope η_α is chosen to be sufficiently negative (green dashed lines in Figure 1) to ensure a single intersection with T_S despite the S-loop. Now the equation for the most probable enthalpy, $T_\alpha(H^*) = T_S(H^*)$, has a single solution, and the enthalpy distribution becomes unimodal. The coexisting states are robustly sampled and, by varying the intercept λ_α , the coexistence range is spanned with multiple replicas.

The effective replica temperature is $T_\alpha(H_\alpha^*)$, and in some cases this corresponds to deep supercooling or superheating; thus, one might be tempted to say that our approach is no different from the conventional one. The point is that the deeply supercooled or superheated states are in equilibrium in the gREM ensemble, or at least in quasi-equilibrium, within a distinct enthalpy landscape metabasin containing a subset of states with the selected enthalpy and not unstable or metastable with respect to another phase with quite different enthalpy as in a constant- T algorithm.

The upshot is that via λ_α enthalpy, not temperature, becomes the control variable, and it is possible to trace a pathway through the transition region without supercooling or superheating. The non-Boltzmann sampling weight, $W(H; \lambda_\alpha)$, is mapped to the ensemble temperature as follows

$$W(H; \lambda_\alpha) = e^{-w_\alpha(H)}, w_\alpha = \int^H \frac{dH'}{k_B T_\alpha(H')} \quad (2)$$

and consequently, differentiating w_α with respect to its upper limit of integration, $dw_\alpha(H)/dH = 1/(k_B T_\alpha(H))$. The integral is calculated over the studied range of enthalpy.

The MD gREM. The gREM was initially implemented as a Monte Carlo (MC) algorithm for both isochoric and isobaric conditions. At constant volume, one simply chooses the acceptance probability for moves of the atom positions so that the weight, $W(U; \lambda_\alpha)$, is sampled instead of the Boltzmann weight.^{2–4} At constant pressure, MC moves in volume V are added, and the acceptance probability is chosen so that the weight, $W(H; \lambda_\alpha)$, is sampled.⁵

Often, a molecular dynamics (MD) algorithm is more efficient than MC. An isochoric MD gREM is made as follows.

A canonical simulation at temperature T_0 samples weight $\exp(-\beta_0 \mathcal{H})$, where $\mathcal{H} = U + \text{KE}$, KE is the kinetic energy, and $\beta_0 = 1/(k_B T_0)$. If the potential is replaced by the effective potential, $U \rightarrow k_B T_0 w_\alpha(U)$, the configurational weight will be $W(U; \lambda_\alpha)$ (eq 2), whereas the velocities are sampled as usual at T_0 with Boltzmann weight.

To derive the forces, F , for a simulation with the effective potential, we note that

$$\frac{dU}{dr} \rightarrow k_B T_0 \frac{dw_\alpha(U)}{dr} = k_B T_0 \frac{dw_\alpha(U)}{dU} \frac{dU}{dr} = \frac{T_0}{T_\alpha(U)} \frac{dU}{dr} \quad (3)$$

and obtain the scaling, $F \rightarrow (T_0/T_\alpha(U)) F$.

Thus, all that is needed to obtain the isochoric MD gREM for a system with potential U is a standard canonical MD simulation at T_0 with scaling of the forces by the factor $s_\alpha(U) = T_0/T_\alpha(U)$.

For the isobaric MD gREM, we combine the above idea with the method of Andersen for conventional isothermal–isobaric MD.⁶ Atom coordinates normalized to the box length $\rho = r/V^{1/3}$ are introduced, and the volume is an additional coordinate. Equations of motion for ρ , V , and for their conjugate momenta are derived from Hamiltonian $\mathcal{H} = U + pV + \text{KE}$, which are then transformed back to equations for r , velocities $v = \dot{r}$, and the time derivative of the volume \dot{V} . The equation for \dot{V} defines the barostat. It is shown in ref 7 that the sampling weight of a trajectory is $\exp(-\beta_0 \mathcal{H})$.

We consider instead the following generalized Hamiltonian, $\mathcal{H} = k_B T_0 w_\alpha(H) + \text{KE}$. The configurational sampling weight is the desired $W(H; \lambda_\alpha)$, whereas the velocities are sampled as usual at T_0 . The equations of motion are generated from a standard isothermal–isobaric algorithm with two changes. First, the forces are scaled by $s_\alpha(H)$ with H replacing U as isochoric conditions are changed to isobaric.

Second, the equation for the volume, the barostat equation, becomes

$$M \frac{d^2 V}{dt^2} = -s_\alpha(H)p + [p_{\text{kin}}(\{\mathbf{v}\}, V) + s_\alpha(H)p_{\text{vir}}(\{\mathbf{r}\}, V)] \quad (4)$$

where M is the fictitious mass associated with the volume and p_{kin} and p_{vir} are the two contributions to the instantaneous internal pressure, the kinetic (ideal gas), and virial (from forces) pressures. Eq 4 differs from eq 3.14c of ref 6 by the presence of the scaling factors. The virial pressure and the barostat pressure, p , are scaled.

A slight rewriting gives

$$\frac{M}{s_\alpha(H)} \frac{d^2 V}{dt^2} = -p + \left[\frac{p_{\text{kin}}(\{\mathbf{v}\}, V)}{s_\alpha(H)} + p_{\text{vir}}(\{\mathbf{r}\}, V) \right] \quad (5)$$

which is the barostat equation.

The factor of $s_\alpha^{-1}(H)$ multiplying the LHS of eq 5 can be considered to produce an enthalpy-dependent mass for the volume, which will cause a H -dependent variation in the time scale of volume fluctuations. However, considering that M is fictitious, this is irrelevant for equilibrium sampling so long as the barostat is numerically functional. Furthermore, despite the presence of time in the MD gREM, we use it for equilibrium sampling only. Then, an inverse scaling of the kinetic ideal gas pressure is all that is required.

Dividing the kinetic pressure by $s_\alpha(H)$ converts T_0 in its average to $T_\alpha(H)$, an appealing confirmation that $T_\alpha(H)$ is the meaningful temperature for the algorithm; it controls the configurational sampling that determines the virial and is the temperature of the ideal gas that gives the kinetic pressure.

In sum, our MD gREM algorithms are built upon conventional MD simulations at T_0 with:

isochoric ensemble

- forces scaled by $s_\alpha(U)$

isobaric ensemble

- forces scaled by $s_\alpha(H)$
- kinetic pressure in the barostat scaled by $s_\alpha^{-1}(H)$

The methods were implemented by our group as a module in LAMMPS,^{8,9} and the isobaric version was applied to gas hydrates.¹⁰ In this paper, it is used to study the liquid \leftrightarrow solid transition in water. A constant pressure algorithm is essential because of the substantial volume change at the transition.

METHODOLOGY

We proceed with the general scheme for the study of phase equilibrium proposed in our earlier work:¹⁰

1. Perform MD gREM simulations with multiple replicas.^{10,11}
2. Calculate the statistical temperature, $T_S(H)$, from replica enthalpy histograms with our statistical temperature weighted histogram analysis method (ST-WHAM).¹² ST-WHAM is an efficient alternative to the usual WHAM¹³ used to combine results from multiple replicas with unknown partition functions, which must be determined iteratively. WHAM converges slowly with increasing system size, whereas ST-WHAM is formulated in terms of intensive properties (instead of extensive) and is iteration free.
3. Describe the transition in terms of the entropy^{10,14–16} computed from integration of $\beta_S(H) = 1/T_S(H)$. A Maxwell construction on $\beta_S(H)$ gives the transition temperature, T_{eq} , and peaks in its derivative, $\gamma(H) = d\beta_S(H)/dH$, identify the subphase transitions connecting different structures of coexisting phases.

SIMULATION DETAILS

Water molecules were modeled as single-bead particles interacting via a Stillinger–Weber potential¹⁷ with parameters determined by Molinero.¹⁸ Although the mW potential does not seek to provide the most accurate atomistic description of the mysteries of water, it reproduces several properties remarkably well,¹⁸ is computationally convenient, and is an appealing model for the first application of the isobaric MD gREM to aqueous phase equilibrium. Atomistic potentials will be considered in future work.

System size was 3168 molecules for hexagonal ice and 3337 molecules for cubic ice and liquid. MD gREM simulations were performed using non-Hamiltonian equations of motion^{19–22} in LAMMPS.^{8,9} We employed the Nose–Hoover thermostat and barostat, setting the kinetic temperature to 330 K and the pressure to 1 or 200 atm under periodic boundary conditions and with the time step set to 0.01 ps. The Nose–Hoover barostat was modified using the principles derived with the Andersen barostat, which are generally applicable.

The number of replicas varied with the system and also due to special attention paid to regions with subphase transitions, which required more densely placed replicas; in general, we used ~ 50 replicas at a time, shifting the studied enthalpy

range and replica distribution to find optimal conditions. The ST-WHAM method¹² was applied to concatenate data from individual replicas and to construct the complete $T_S(H)$ function. Data gathered before each replica was equilibrated were not included in the final analyses (i.e., data were not taken until spontaneous transitions to more stable subphases were no longer observed).

The gREM module should soon be available in the LAMMPS distribution.

We refer in this manuscript to subphases¹⁶ that are distinct configurations in the coexistence region with, e.g., liquid sphere, cylinder, and slab forming in ice, due to surface effects in the finite simulation box as melting proceeds.

SYMMETRY IDENTIFICATION VIA ORDER PARAMETERS

To distinguish between crystal and liquid phases formed by water molecules interacting via the mW potential, we tested several local bond order parameters, as presented below. We were especially interested in distinguishing between hexagonal ice, cubic ice, and liquid. Order parameters were determined for these three reference types of water. We built boxes of each type and equilibrated them at 290 K and 1 atm in standard isothermal–isobaric NpT simulations to account for fluctuations about the lattice sites of the ices. For each water molecule, neighbors were defined as molecules within a 3.4 Å cutoff to include the first hydration shell.

Although 290 K is above the T_{eq} , it is well below the limit of ice stability of ~ 340 K and easily simulated. It represents an attempt to include the fluctuations needed to describe the high- T_S part of the coexistence region without going too far above T_{eq} and to obtain the regions of order parameter space corresponding to the different phases for the entire coexistence region. The order parameters we considered are as follows:

Number of Nearest Neighbors (nn). nn is not useful in the present analysis because it is the same for both types of ice and for liquid water, and fluctuations were not strong enough to allow type assignment.

Steinhardt Order Parameter (q_l).²³ q_l is based on the arrangement of the nearest neighbors of particle i , obtained by placing spherical harmonics, Y_{lm} , on the neighbors, and calculating the following

$$q_l(i) = \sqrt{\frac{4\pi}{2l+1}} \sum_{m=-l}^l |q_{lm}(i)|, \quad q_{lm}(i) = \frac{1}{N(i)} \sum_{j=1}^{N(i)} Y_{lm}(\hat{r}_{ij})$$

where $N(i)$ is the number of nearest neighbors around particle i . We utilized q_3 , q_4 , and q_6 .

Averaged Bond Parameters. These parameters were introduced by Lechner and Dellago²⁴ and are a modification of the Steinhardt order parameter, where instead of only the first hydration shell, the arrangement of the first and second shell is taken into account

$$\langle q_l \rangle(i) = \sqrt{\frac{4\pi}{2l+1}} \sum_{m=-l}^l |\bar{q}_{lm}(i)|, \quad \bar{q}_{lm}(i) = \frac{1}{\bar{N}(i)} \sum_{j=1}^{\bar{N}(i)} q_{lm}(k)$$

The sum in the last equation runs over all neighbors of particle i as well as particle i itself. According to the authors, the averaged bond parameters allow for a clearer distinction between different phases for particles interacting via Lennard–Jones and Gaussian core potentials. We tested three of the

averaged local bond order parameters, $\langle q_3 \rangle$, $\langle q_4 \rangle$, $\langle q_6 \rangle$, extending code provided by Lechner.²⁵

Order Parameters Used by Galli. This is another modification of the Steinhardt order parameter²⁶

$$q_l^G(i) = \frac{1}{N(i)} \sum_{j=1}^{N(i)} \frac{\sum_{m=-l}^l q_{lm}(i) q_{lm}^*(j)}{\sqrt{\sum_{m=-l}^l q_{lm}(i) q_{lm}^*(i)} \sqrt{\sum_{m=-l}^l q_{lm}(j) q_{lm}^*(j)}}$$

We tested two of these parameters, namely, q_3^G and q_6^G .

There are also other versions of the Steinhardt order parameters, e.g., those used in the CHILL algorithm.²⁷ However, in CHILL, apart from calculating values of two order parameters for each molecule, one needs to go through a second round and analyze each particle with respect to the symmetries of its neighbors. Therefore, we sought an algorithm that compares values assigned to a chosen molecule only, with the idea that an optimal pair of order parameters would contain enough information about the molecule and its nearest neighbors to assign the phases.

The Best Set of Order Parameters. For eight considered order parameters (q_3 , q_4 , q_6 , $\langle q_3 \rangle$, $\langle q_4 \rangle$, $\langle q_6 \rangle$), we sought the best pair to distinguish cubic ice, hexagonal ice, and liquid water. We found six possible pairs that could be used to create an algorithm for symmetry determination (see details in [Supporting Information](#)) and finally decided upon $(q_3^G, \langle q_6 \rangle)$.

Figure 2 presents the lowest contour lines on 2D scatter plots for q_3^G versus $\langle q_6 \rangle$, for all three types of water molecules.

We used linear functions to divide the q_3^G – $\langle q_6 \rangle$ plane into regions occupied by each symmetry type according to the following recipe

```

if  $\langle q_6 \rangle > 0.1 q_3^G + 0.44$ 
     $\langle q_6 \rangle < -2.2 q_3^G - 1.37$  cubic
else if  $\langle q_6 \rangle > 0.1 q_3^G + 0.44$ 
     $\langle q_6 \rangle > -2.2 q_3^G - 1.37$ 
     $\langle q_6 \rangle < -2.2 q_3^G - 0.9$  hexagonal
else if  $\langle q_6 \rangle < 0.1 q_3^G + 0.44$ 
     $\langle q_6 \rangle < -0.12 q_3^G + 0.33$ 
     $\langle q_6 \rangle > -1.08 q_3^G - 0.6$  liquid
else unassigned

```

We propose the above algorithm to assign type to water molecules modeled via the mW potential. We used it in the analysis of all of our simulations.

■ ICE MELTING

Hexagonal ice is the thermodynamically stable form of ice under conditions usually observed on Earth's surface, whereas cubic ice is proposed to be naturally formed in high clouds. In the present paper, we employed the isobaric MD gREM to study melting of both types of ice to compare their properties.

Snapshots of stable and topologically different structures observed during ice melting under 1 atm are shown in [Figure 3](#). With every replica initialized as ice, these structures have reached equilibrium under gREM sampling, in sharp contrast to what is found in a constant- T algorithm with an irreversible process following superheating that leads to a fully liquid system.

The observed sequence of structures for both types of ice with enthalpy, the control variable, increasing left to right, is

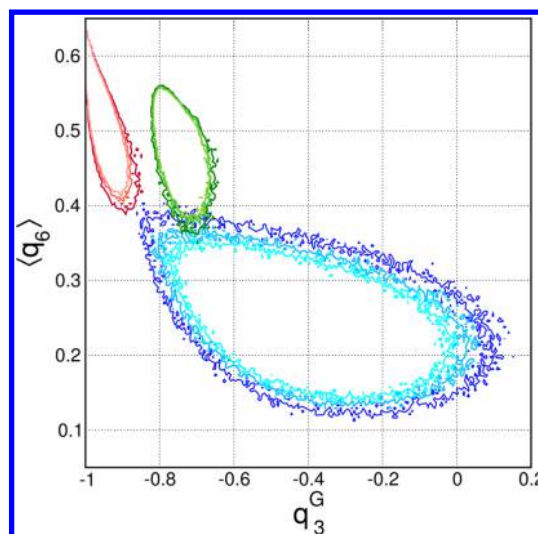


Figure 2. Raw (not smoothed) contour lines of 2D scatter plot of values of order parameters q_3^G and $\langle q_6 \rangle$ with blue for liquid water, green for hexagonal ice, and red for cubic ice. Color shades from darkest to lightest correspond to 1, 2, or 3 particles in a bin for bins of size 0.01. Contours for higher values are not shown for clarity. Phases are well-separated with small overlap between liquid and hexagonal ice.

similar to that in β ice melting¹⁰ and in Lennard-Jones fluids,²⁸ suggesting that the presence of many “subphases”¹⁶ is a general property.

Adding heat to a box of ice leads first to formation of a liquid ball, then to a liquid cylinder, followed by ice and liquid slabs, ice cylinder in liquid, and finally a fully liquid system. A similar sequence was observed for both kinds of ice under 200 atm. This is a pattern similar to that described by Binder et al.^{28,29} in liquid \leftrightarrow vapor transitions using density as the control variable. The formation of a liquid ball is an example of the droplet evaporation/condensation transition.

The statistical temperature curves calculated for hexagonal and cubic ice under 1 atm are presented in panels (a) of [Figures 4](#) and [5](#), respectively. Each transition between topologically different structures is connected with a feature in the statistical temperature, making $T_S(H)$ more complex than just a simple S-loop.^{14–16}

We employed the entropic analysis outlined above, and its results are shown in the other panels of [Figures 4](#) and [5](#). Numerical values of the calculated properties of both systems are presented in [Tables 1](#) and [2](#). Random error was estimated by dividing our data into 10 subsets, calculating the reported quantities in each, and conservatively using half of the difference between the smallest and largest value as the error estimate.

The melting temperature, T_{eq} , was calculated via the Maxwell construction, which in the entropic approach takes the form of an equal-area construction on $\beta_S(H)$, which is the inverse of $T_S(H)$ (see panels (b) in [Figures 4](#) and [5](#)). In both cases, the melting temperature is overlapping with a plateau in the statistical temperature where slabs of ice and liquid coexist. In fact, melting of an ice layer in the slab configuration does not require formation of a new surface (in contrast to, e.g., formation of a liquid ball in an ice box), and therefore, there are no surface effects on the behavior of T_S . Ice melting can maintain constant temperature in this region, as expected in an infinite system. The location of such

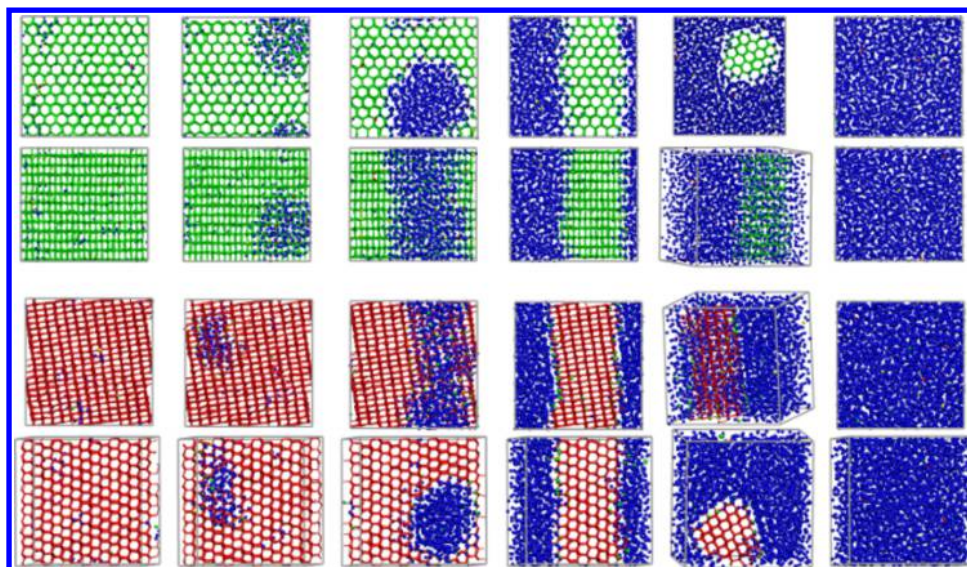


Figure 3. Snapshots of representative equilibrium configurations observed during the transition from hexagonal (top) or cubic ice (bottom) to liquid water under 1 atm with each structure shown from two points of view for easier identification of structural topology. Blue represents liquid, green and red are for hexagonal and cubic ice, respectively, molecules with unassigned type are yellow. From left to right: ice, ice with liquid ball, ice with liquid cylinder, ice and liquid slabs, ice cylinder in liquid, and liquid. Control variable enthalpy increases left to right.

a plateau is an effective estimator of the transition temperature, and coincidence with the temperature from the Maxwell construction gives added confidence.

For hexagonal ice/liquid at 1 atm, the calculated melting temperature and latent heat from the difference of the enthalpies of the coexisting phases are the same as earlier reported values.¹⁸ The ΔV of melting of hexagonal ice¹⁸ is smaller than that of the experimental data. Using it with the Clapeyron equation and our computed ΔH and T_{eq} , we find that T_{eq} should fall by 0.4 K upon raising the pressure to 200 atm; our simulations show a drop of 0.3 K, which is within the uncertainty.

The derivative of $\beta_S(H)$, $\beta'_S(H) = \partial\beta_S/\partial H$, is useful in analyzing locations of subphase transitions and their order.¹⁶ If a peak (a maximum) in β'_S has a positive value, the corresponding transition is of the first order, otherwise, it is second order. In the cases of hexagonal and cubic ice, all observed transitions between subphases are first order.

The entropy, $S(H)$, can be easily calculated to within an additive constant from the statistical temperature as

$$S(H) = \int^H \frac{1}{T_S(H')} dH' \quad (6)$$

and it is shown in black in panels (d) in Figures 4 and 5. The integration is from an arbitrary point in the studied enthalpy range to a variable upper limit. The choice of the lower limit determines an additive constant in the entropy as a function of enthalpy. The convex character of the entropy in the transition region is shown insofar as it falls below the Gibbs hull, $S^G(H) = S(H_1) + (H - H_1)/T_{eq}$, a straight line tangent to $S(H)$ at H_1 and H_2 (cyan line). The maximal difference between the entropy and the Gibbs hull is the surface entropy, ΔS_{surf} , and is a measure of the strength of the surface effects causing the S-loop in T_S .

Specifically, ΔS_{surf} provides an estimate of the surface tension, γ ,

$$\gamma = \frac{T_{eq} \Delta S_{surf}}{\sigma}$$

where σ is the surface area between the phases. Here, the surface entropy is evaluated at an enthalpy where the system is in the slab configuration (see its location in panels (d) in Figures 4 and 5), and therefore, σ can be estimated as $2L^2$, where L is the box size, and the 2 is a result of having two surfaces with periodic boundary conditions.

Values of the surface tension obtained at T_{eq} for hexagonal ice/liquid are in agreement with published experimental values at the melting temperature: 29.1 ± 0.8 mJ/m²,³⁰ 31.7 ± 2.7 mJ/m², respectively;³¹ a more detailed list can be found elsewhere.^{32,33} A value of 21.6 mJ/m² for cubic ice/liquid at 200 K was derived for clusters of water produced by condensation of vapor in supersonic flow, based on an approximate kinetic theory of nucleation, and was substantially lower than the hexagonal/liquid surface tension at 0 °C.³⁴ This trend is also found in our calculations where, for both studied pressures, the surface tension for cubic ice/liquid is significantly lower than for hexagonal ice/liquid, 23.6 versus 30.8 mJ/m² for 1 atm and 24.1 versus 30.3 mJ/m² for 200 atm, respectively.

During melting of hexagonal ice, we observed that the secondary-prism face was exposed to the liquid phase, just as reported earlier.^{35,36}

Finally, with the entropy in hand, one can calculate the Gibbs free energy profile at the transition temperature as $G(H) = H - T_{eq}S(H)$, as presented in panels (e) in Figures 4 and 5. The barrier connects the homogeneous liquid and ice phases on either end of the transition region. It is not the nucleation barrier but is a result of surface effects in the simulation box. The temperature-dependent quantity, available as $G(T_S) = H(T_S) - T_S S(H(T_S))$ (in the Supporting Information), is triple-valued in the transition region, confirming that a simpler picture is obtained with H as the control variable.

Figure 6 compares the stability of the two ices via their $G(H)$ profiles calculated at the transition temperature of cubic

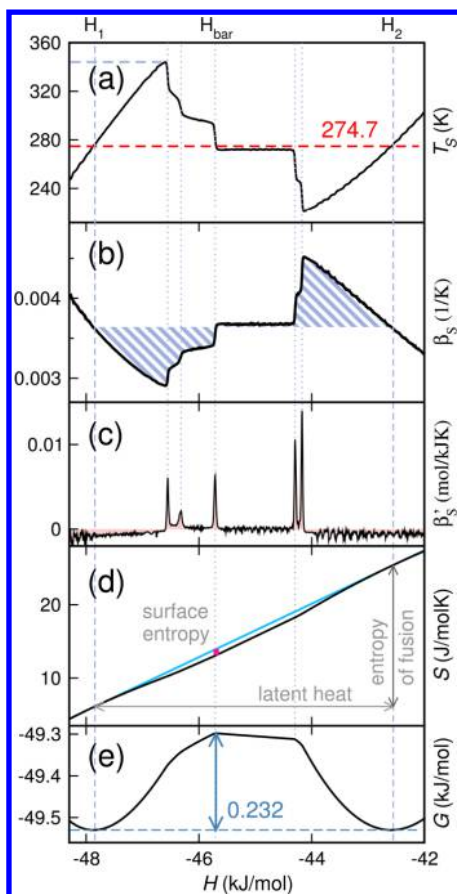


Figure 4. Entropic analysis of the melting of hexagonal ice under 1 atm with each replica initialized as hexagonal ice. (a) The statistical temperature, $T_S(H)$, is in black, and the transition temperature, T_{eq} , is the dashed red line. The limit of stability of ice is shown in blue. (b) The inverse of the statistical temperature, β_S , with shaded equal areas used in the Maxwell construction to determine T_{eq} . (c) Peaks in β_S were used to locate transitions between subphases. (d) Entropy is shown as black, Gibbs hull as cyan, and surface entropy as red. Arrows represent latent heat and entropy of fusion. (e) Free energy profile at T_{eq} .

ice (top) and hexagonal ice (bottom). Entropy is obtained to within an additive constant by eq 6. To have the same value of this constant for both ices, and to get positive values of entropy across the coexistence region, we start the integration at high enthalpy, where both systems are identical liquid water and the T_S curves overlap, and shift the entropy curves up by 2 eV. The entropies are also identical at high enthalpy. Figure 6 expresses the correct free energy differences, but because of the constant, not the absolute values.

Both the top and bottom panels show that the free energy of hexagonal ice, corresponding to the solid branch, low enthalpy minimum, is lower than the free energy of cubic ice, as expected because hexagonal ice is indeed the stable phase. The difference in free energies at either melting temperature is ~ 0.1 kJ/mol.

As a check on the estimate of the free energy difference, note that because the free energies of ice and liquid are equal at the melting temperature, $G_c(269.0 \text{ K}) - G_h(274.7 \text{ K}) = S_l \times (274.7 - 269.0)$, assuming the liquid entropy is constant over the small temperature range. Subscripts c, h, and l refer to cubic ice, hexagonal ice, and liquid, respectively. Adding the excess entropy of mW [35] to the entropy of a monatomic

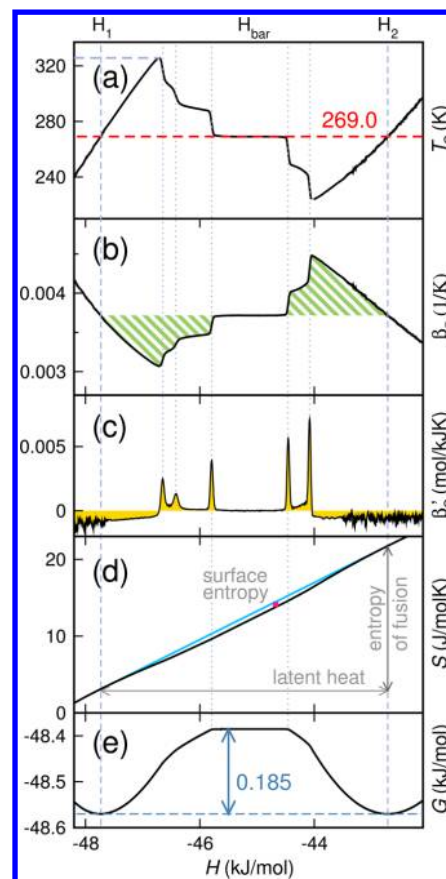


Figure 5. Entropic analysis for melting of cubic ice presented as for hexagonal ice in Figure 4.

Table 1. Characteristics of the Melting of Hexagonal and Cubic Ice at 1 atm with Error Estimates Shown in Parentheses

	hexagonal ice	cubic ice
melting temperature T_{eq} (K)	274.7 (0.1)	269.0 (0.1)
number of stable subphases	6	6
surface entropy (J/mol K)	0.842 (0.002)	0.688 (0.002)
entropy of fusion (J/mol K)	19.2 (0.1)	18.6 (0.1)
latent heat (kJ/mol)	5.29 (0.02)	5.01 (0.03)
free energy barrier (kJ/mol)	0.232 (0.001)	0.185 (0.001)
surface tension (mJ/m ²)	30.88 (0.08)	23.65 (0.06)
limit of ice stability (K)	344.0 (0.2)	325.6 (0.6)

Table 2. Characteristics of the Melting of Hexagonal and Cubic Ice at 200 atm

	hexagonal ice	cubic ice
melting temperature T_{eq} (K)	274.4 (0.2)	268.3 (0.1)
number of stable subphases	6	6
surface entropy (J/mol K)	0.83 (0.01)	0.703 (0.003)
entropy of fusion (kJ/mol K)	19.2 (0.1)	18.6 (0.1)
latent heat (kJ/mol)	5.26 (0.03)	5.00 (0.01)
free energy barrier (kJ/mol)	0.229 (0.003)	0.189 (0.001)
surface tension (mJ/m ²)	30.3 (0.4)	24.07 (0.09)
limit of ice stability (K)	345.9 (1)	326.5 (0.6)

ideal gas with the mass of water at the same temperature and density of the liquid, one finds $S_l \approx 55 \text{ J}/(\text{mol K})$, and

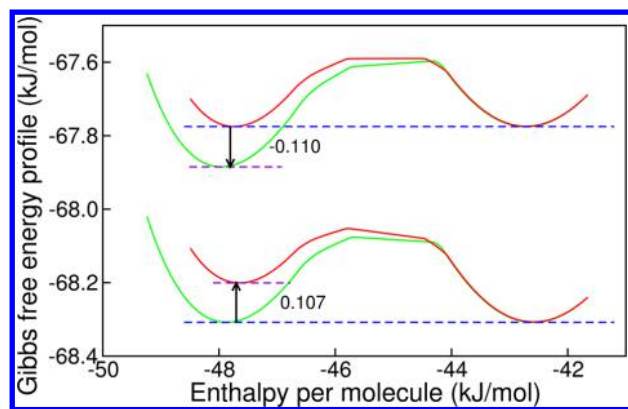


Figure 6. Gibbs free energy profiles for hexagonal (green) and cubic (red) ice melting under 1 atm at T_{eq} of cubic ice (top two curves) and at T_{eq} of hexagonal ice (bottom two curves). Dashed lines indicate the equal depths of the minima of the ice at its transition temperature.

$G_c(269.0 \text{ K}) - G_h(274.7 \text{ K}) \approx 313 \text{ J}/(\text{mol K})$ (we thank the referee for this argument).

Now consider evaluating the free energy difference at the respective melting temperatures by first converting hexagonal ice to cubic ice at 274.7 K, the process that we considered, and then cooling cubic ice to 269.0 K: $G_c(269.0 \text{ K}) - G_h(274.7 \text{ K}) = 107 \text{ J}/(\text{mol K}) + S_c \times (274.7 - 269.0)$. For the second step, S_c is estimated as the 55 $\text{J mol}^{-1} \text{ K}^{-1}$ of the liquid minus the entropy of fusion, $5014/269 = 18.6 \text{ J mol}^{-1} \text{ K}^{-1}$, and $S_c \approx 36.4 \text{ J mol}^{-1} \text{ K}^{-1}$. We obtain $G_c(269.0 \text{ K}) - G_h(274.7 \text{ K}) \approx 314 \text{ J mol}^{-1} \text{ K}^{-1}$, in perfect agreement with the first estimate. Thus, $G_c - G_h$ being $\approx 110 \text{ J/mol}$ at either melting temperature, and $\approx 313 \text{ J/mol}$ between the respective melting temperatures, is perfectly consistent.

■ WATER FREEZING AND HYSTERESIS

To study water freezing, we initiated all replicas with liquid configurations. Figure 7 compares T_S curves for liquid water

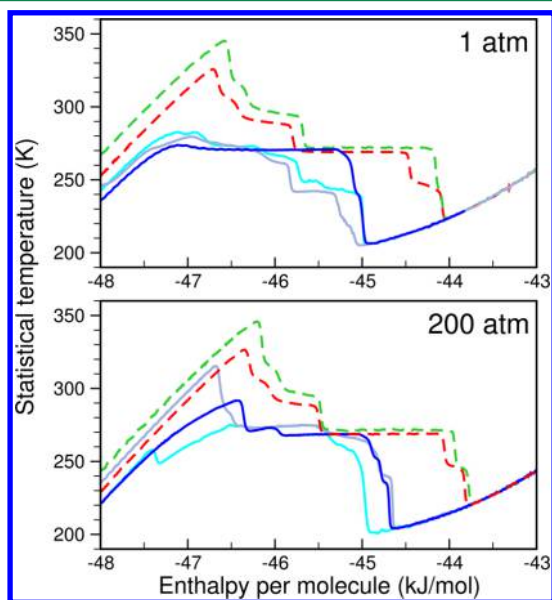


Figure 7. Distinct statistical temperatures for water freezing (three solid blue shades) versus melting of hexagonal (dashed green) and cubic ice (dashed red) under 1 atm (top) and 200 atm (bottom).

freezing (solid lines) and ice melting (dashed lines). Now, in contrast to melting, different initial conditions like the random seed for the velocity generation or a different set of effective temperatures $\{T_\alpha\}$ lead to different results, i.e., multiple T_S curves as shown. The T_S curves for freezing are broadly reproducible but exhibit run-to-run fluctuations, whereas the T_S for ice melting of both types of ice are perfectly reproducible.

Nevertheless, some general features of the freezing curves are preserved and allow comparison with those for melting. The pure liquid branches of T_S for both freezing and melting overlap at temperatures above 240 K, and there is partial overlap in the coexisting slab region. The largest differences between melting and freezing appear in the supercooled region near the minimum in T_S and in the superheated region near the maximum. The limits of stability for supercooled water freezing are equal to 206 K under 1 atm and 204 K under 200 atm (value of 205 K under 1 atm was reported by Molinero¹⁸) and lie much below the minimum in T_S observed during ice melting. The limit of stability for superheated ice melting lies above the maximum in T_S observed during freezing. Corresponding values are presented in Table 1.

In short, we observe hysteresis in the statistical temperature, indicating broken ergodicity, which is not surprising. Freezing and melting require symmetry making and breaking, respectively. With hexagonal or cubic ice already in place for melting, it is difficult for the system to find configurations with a different solid symmetry, or the most deeply supercooled liquid states.

For freezing, by contrast, there is no crystallite already present and no predisposition to a particular symmetry, the process is sensitive to the fluctuations in the nucleus formation, and either, or mixed, symmetry structures can form, as seen in Figure 8 via representative structures across the coexistence region.

The gREM is designed to sample configurations in equilibrium from a small part of the T_S curve. For the simpler liquid–vapor transition, there are no complications. However, with a symmetry change and the presence of multiple solid types, we now see a picture of distinct, well-separated metabasins with characteristic T_S curves that do not allow exchange on the time scale of our simulations—the essence of hysteresis. The gREM can trace a path along a given T_S but cannot find a single path corresponding to complete equilibrium in the generalized ensemble. Fortunately, such is also the case in experiments where the configurations sampled along a growth pathway are kinetically controlled.

Turning to the solid side of the T_S curves, for a given temperature, hexagonal ice (green dashed lines) has the lowest enthalpy and then cubic (red dashed lines); ice formed by water freezing (solid blue lines) is highest.

For a different slant on stability, the presence of multiple T_S at a single H may be interpreted with Stillinger's inherent structure (IS) theory.³⁷ The multidimensional enthalpy landscape is partitioned into the domains of attraction of its local minima, configurations denoted IS. The enthalpy of a configuration is the enthalpy of the IS for the basin to which it belongs, plus the “vibrational” enthalpy, the excitation above the minimum. With approximate equipartition, the kinetic energy, and thus T_S , is proportional to the vibrational enthalpy.³⁸ Therefore, a given H may arise from a deep basin (low-lying IS) and a high vibrational excitation, and T_S ,

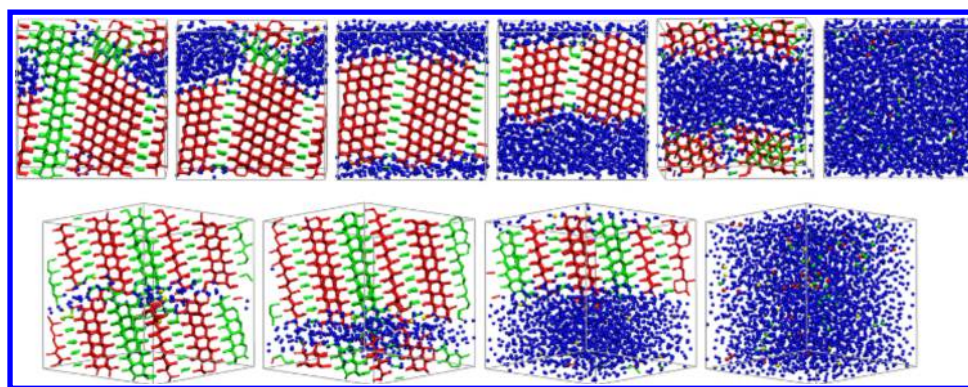


Figure 8. Representative configurations across the transition region during water freezing with decreasing enthalpy from right to left under 1 atm (top) and 200 atm (bottom). Blue represents liquid; green and red are for hexagonal and cubic ice, respectively, and unassigned are yellow.

or a shallow basin and a small excitation, and T_S . From this viewpoint we see again that the structure with the highest T_S , hexagonal ice, has the deepest, most stable basin, and so forth.

What Kind of Ice Is Formed Upon mW Water Freezing? Snapshots of stable structures observed during ice formation under 1 and 200 atm across the transition region are shown in Figure 8. Instead of forming hexagonal ice immediately, a layered mixture of hexagonal and cubic ice is initially formed and then stabilized with decreasing enthalpy (moving toward the solid side of the $T_S(H)$, Figure 7). Such layered ice was named stacking disordered ice I or I_{sd} by Malkin et al.³⁹ in 2012. A short review of the history of its discovery is presented in ref 40.

The finding of the ice I_{sd} started with unexpected neutron diffraction patterns of cubic ice published by Kuhn et al.⁴¹ in 1987 and was later confirmed both experimentally and computationally.^{26,27,39–49} Molinero studied its growth in deeply supercooled water at 180 K using the mW model⁴⁵ and observed layers at a ratio of 2 to 1 for cubic and hexagonal ice, whereas Galli et al.,²⁶ for the same model at 220–240 K, found that the critical nucleus is a mixture of both in equal proportions. Malkin et al. observed a ratio of 1:1 for TIP4P water at 220 K.⁴⁰

According to recent results of Quigley,⁵⁰ the mW model forms layered ice more easily than hexagonal ice over the entire supercooled region, independent of nucleus size, and the process is thermodynamically controlled. However, the majority of other results suggest that it is kinetics of the growth in nonequilibrium conditions that control the layered ice formation.^{26,27,39,45}

In our simulations, the composition of the layered ice depends on starting conditions (number of replicas, values of intercept, random number seed for velocities). Different arrangements of layers were formed with varying ratios of both types of ice leading to multiple branches of $T_S(H)$, as shown in Figure 7. Also, each mixture was stable in our simulations, confirming the observation that the Gibbs free energy difference between pure hexagonal or cubic ice and I_{sd} is small.^{42,45,51} We conclude that the initial stage of mW ice formation is kinetically controlled.

None of the structures presented in Figure 8 consist of only hexagonal ice. With decreasing intercept in $T_\alpha(H)$, in replicas crossing T_S where it corresponds to a solid phase, we observe that the amount of hexagonal ice indeed increases. However, we expect to see full transformation into hexagonal ice after much longer equilibration times. A long time is needed for

full rearrangement of the hydrogen bond network, even using the enhanced sampling of the MD gREM.

Figure 9 presents changes in the normalized population of all types of water across the replicas spanning the transition

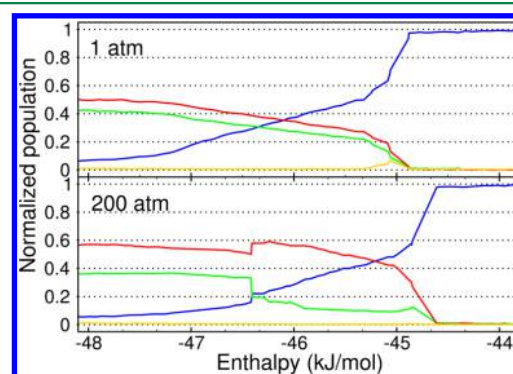


Figure 9. Normalized population of liquid water (blue), hexagonal ice (green), cubic ice (red), and unassigned molecules (yellow) across the transition region for water freezing under 1 (top) and 200 atm (bottom), as a function of enthalpy. Data were averaged for two chosen runs, one for each pressure, over six sets of frames, one from each replica, collected every 10 ns.

region for water freezing under 1 and 200 atm as a function of the most probable enthalpy observed in the replicas. The amount of liquid water, taking almost the entire box on the liquid side of $T_S(H)$, suddenly drops to around 55% when ice is formed and ice/liquid slabs are the equilibrated structures, then linearly decreases in the plateau region, and finally reaches less than 10% after reaching the solid side of $T_S(H)$. The ices obviously present the opposite trend. Interesting behavior is observed under 1 atm where water freezes; apart from changes in the amounts of liquid and ice, there is a significant increase in the amount of unassigned water, suggesting that ice nucleation goes through more complex structures.

The present manuscript is focused on equilibrium across the coexistence region, but we would like to use our methods to advance nucleation theory to examine the pathway for the formation of the critical ice nucleus. The ice ball formed upon freezing is not the critical nucleus but is rather an equilibrium structure governed by finite size effects.^{28,29} However, nucleation occurs somewhere along the nearly vertical segment of T_S leading from the supercooled liquid to the

ball, ≈ -45 kJ/mol at 1 atm, providing a good starting point for other studies.

The lower surface tension of cubic ice compared to hexagonal ice could be responsible for the formation of layered ice instead of thermodynamically stable hexagonal ice in the initial stages of freezing. One might ask why cubic ice is not even more prevalent. Note that we are not studying nucleation, but growth after nucleation has occurred via well-equilibrated coexisting states. Thus, we do not show the very earliest stages of the process. In fact, the snapshots closest to nucleation show a greater preponderance of cubic than does that of Figure 9.

■ PERFORMANCE OF THE MD GREM

The gREM was designed to deal with barriers in first order phase transitions and sample the coexisting states. Are these goals being met?

Values of the slope, η_ω , and the intercept, λ_ω of the effective temperature, T_ω determine where the effective temperature will intersect the statistical temperature and if it will intersect only once, as required. The steepness of T_α must increase as does that of T_S . Slope values between -2 and -6 give enough steepness to T_α for the majority of the coexistence range, giving at the same time reasonably wide enthalpy distributions in each replica.

However, such is not the case around a subphase transition and the associated barrier, where $T_S(H)$ is nearly vertical. Nevertheless, we do not resort to extremely steep $T_\alpha(H)$, as this leads to narrower enthalpy distributions, an increased number of replicas required to cover the interesting enthalpy range, greater sensitivity to fluctuations, and subsequently, to increased computational cost and numerical instability of the algorithm. We used the same value of η for all replicas, although this value was changed from -2 to -6 after initial calculations.

The above considerations help explain our findings about sampling of the coexistence region. Broadly, by varying both parameters, η_ω and λ_ω we find that it is indeed possible to obtain reasonably flat combined enthalpy histograms, i.e., good sampling. An example for water freezing under 1 atm is shown in Figure 10.

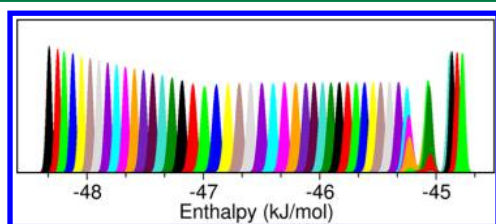


Figure 10. Enthalpy histograms for water freezing under 1 atm with replica effective temperatures chosen to uniformly cover the coexistence range.

Now, consider the barrier regions separating subphases. Figure 11, bottom, shows an example of enthalpy histograms for melting of cubic ice. Except for regions around the four barriers, the combined enthalpy distribution is flat. Around the barriers, however, we observe depletion of the sampled states. Nevertheless, the MD gREM, without extremely steep T_ω is successfully exchanging replicas around the barriers and reducing the problem of broken ergodicity, as is seen in the three top panels of Figure 11, presenting the time-dependent

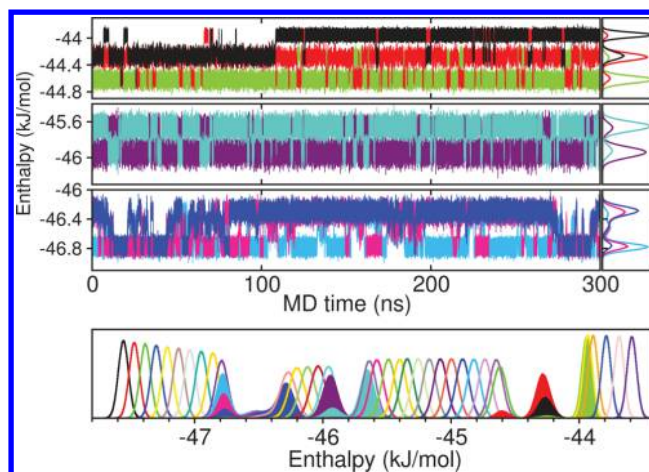


Figure 11. Enthalpies and enthalpy histograms of MD gREM replicas for cubic ice melting under 1 atm. Top three panels: enthalpies observed around (i) ice slab \leftrightarrow ice cylinder \leftrightarrow liquid, (ii) liquid cylinder \leftrightarrow ice slab, (iii) ice \leftrightarrow liquid ball \leftrightarrow ice slab. Bottom: enthalpy histograms with solid colors for replicas around barriers, showing efficient replica exchange across all barriers.

enthalpies. Figure 12 shows a single replica sampling three topologically different states and as such overcoming two close lying barriers.

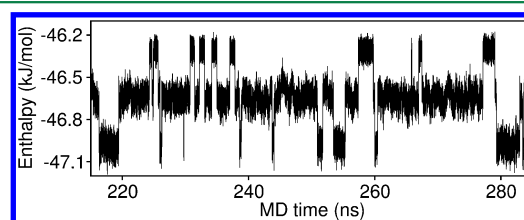


Figure 12. Enthalpy changes due to replica exchanges in one of the replicas for cubic ice melting. Configurations sampled in this replica frequently changed according to ice slab \leftrightarrow ice cylinder \leftrightarrow liquid.

Figure 13 shows enthalpy versus time in a set of replicas initialized with liquid configurations and with effective

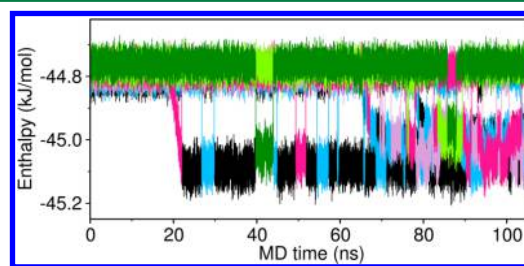


Figure 13. Multiple spontaneous water freezing events under 200 atm in gREM replicas around the homogeneous nucleation point.

temperatures chosen to sample a narrow range of statistical temperature around the homogeneous nucleation point, i.e., the minimum of T_S . First, it shows multiple events of ice formation indicated by a drastic drop in enthalpy. Second, it shows frequent replica exchanges between liquid \leftrightarrow (liquid + ice). The MD gREM is equilibrating and sampling states in a way that is impossible with temperature as the control variable.

We have chosen the slope in T_α such that it is steep enough to ensure a single crossing of the statistical temperature in most of the transition region, but not where T_S is most steep. As a result, around these most steep parts of T_S , T_α is still crossing T_S more than once. An interesting consequence is the presence of two-way spontaneous transitions between significantly different configurations in replicas located on a barrier. That is, the enthalpy distribution is broad enough to encompass states of different types, and transitions between them are observed in equilibrium. Such intrareplica transitions occur along with those from inter-replica exchange. Figure 14 presents an example with S for spontaneous transitions and E for changes in enthalpy caused by replica exchange.

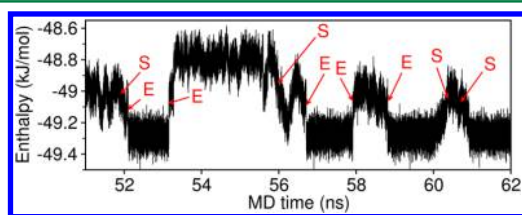


Figure 14. Enthalpy changes, spontaneous (S) and from replica exchange (E), in one the replicas for cubic ice melting.

DISCUSSION

The gREM algorithm was designed to sample in equilibrium the states with coexisting phases along the pathways of first order transitions. Here, the isobaric molecular dynamics version was described and applied to the very interesting and challenging solid \leftrightarrow liquid transition in water.

The performance of the MD gREM in sampling the coexistence region was verified by observing the replica enthalpy histograms and frequency of transitions among configurations in the most hard-to-sample regions. On the whole, the transition region is well-covered. There is a decrease in sampling near some barriers connecting states with different topologies, the subphases, but replica exchanges around the barriers still occur. By contrast, the phase coexistence region would be entirely inaccessible to algorithms with temperature as the control variable.

We have presented an alternative to the usual employment of algorithms with temperature as the control variable in the study of phase transitions. Our approach is to obtain the statistical temperature, $T_S(H)$, from gREM enthalpy histograms with the ST-WHAM method¹² and then apply an entropic analysis.^{14–16}

As the gREM seeks enhanced equilibrium sampling with a non-Boltzmann weight, in simple cases, we expect to describe the system with a single $T_S(H)$ function. However, despite some randomness in the freezing pathways, we overall found distinct, reproducible $T_S(H)$ functions for freezing versus melting.

The configurations in the melting pathway are more ordered, retain the symmetry of the original ice, and take on shapes determined by surface effects, whereas freezing produces more disorder and solid structures with mixtures of hexagonal, cubic, and unassigned molecules. The differences are not surprising in view of the symmetry change and the known differences in the pathways found in experimental and simulation data. From the perspective of equilibrium sampling,

it indicates the presence of distinct groups of states separated by a barrier that will not be surmounted in the accessible simulation time.

The entropic analysis identifies (i) the equilibrium transition temperature via an equal area construction on $\beta'_S(H) = 1/T_S(H)$, (ii) the latent heat from the difference of the enthalpies of the coexisting states found in the equal-area construction, (iii) subphase transitions between distinct structures via peaks in $\beta'_S(H)$, and (iv) the surface tension from the surface entropy. Graphical representations of this analysis are presented in Figures 4 and 5.

As melting of ice does not change its structure and does not introduce competition related to formation of another ice type, it is easier to equilibrate simulations of ice melting than simulations of water freezing. We consider that the $T_S(H)$ for ice melting, with an equal area construction on the corresponding $\beta'_S(H)$, should be used to estimate the transition temperature T_{eq} . Also, the central plateau on such $T_S(H)$ corresponds to a water/ice slab configuration where changing the relative amounts of solid and liquid does not change the surface area. Thus, we also suggested the plateau temperature, for melting, as an estimator of T_{eq} , and that the two estimates should coincide for best confidence. The equal-area and plateau estimates are indeed very close, 274.7 and 272.0 K for hexagonal and 269.0 and 269.0 K for cubic, respectively. We observe excellent agreement for T_{eq} for hexagonal ice melting that was previously given as 274.6 K,¹⁸ and for the latent heat we find 5.26 kJ/mol (1.26 kcal/mol), identical to that previously given.¹⁸

Surface tensions are easily obtained with good agreement with the literature for hexagonal ice/liquid and with new results for cubic ice/liquid, which is not well-known.

The $T_S(H)$ functions for freezing are broadly similar to run-to-run fluctuations. The sampled configurations describe pathways from liquid that will eventually form hexagonal ice, evolving through mixed solid structures of hexagonal and cubic ices. These paths are not the result of deep supercooling into unstable or metastable states with temperature as the control variable, but rather, each enthalpy interval is sampled in quasi-equilibrium. We will examine their connection to experimental data in a subsequent paper.

ASSOCIATED CONTENT

Supporting Information

The Supporting Information is available free of charge on the ACS Publications website at DOI: 10.1021/acs.jctc.5b00637.

Six possible pairs of order parameters that could be used to create an algorithm for symmetry determination and the Gibbs free energy plots for the studied systems (PDF)

AUTHOR INFORMATION

Corresponding Author

*E-mail: keys@bu.edu.

Notes

The authors declare no competing financial interest.

ACKNOWLEDGMENTS

The research was supported by the U.S. Department of Energy, Office of Basic Energy Sciences, Division of Chemical Sciences, Geosciences and Biosciences under Award DE-

SC0008810. We thank Profs. William Klein, Harvey Gould, and Dr. Jaegil Kim for discussions.

REFERENCES

- (1) Matsumoto, M.; Saito, S.; Ohmine, I. *Nature* **2002**, *416*, 409–413.
- (2) Kim, J.; Keyes, T.; Straub, J. E. *J. Chem. Phys.* **2010**, *132*, 224107.
- (3) Terada, Y.; Keyes, T.; Kim, J.; Tokuyama, M. *AIP Conf. Proc.* **2012**, *1518*, 776.
- (4) Lu, Q.; Kim, J.; Straub, J. E. *J. Chem. Phys.* **2013**, *138*, 104119.
- (5) Lu, Q.; Kim, J.; Straub, J. E. *J. Phys. Chem. B* **2012**, *116*, 8654.
- (6) Andersen, H. C. *J. Chem. Phys.* **1980**, *72*, 2384.
- (7) Malolepsza, E.; Secor, M.; Keyes, T. *J. Phys. Chem. B* **2015**, *119*, 13379–13384.
- (8) Plimpton, S. J. *Comput. Phys.* **1995**, *117*, 1–19.
- (9) LAMMPS. <http://lammmps.sandia.gov>.
- (10) Malolepsza, E.; Kim, J.; Keyes, T. *Phys. Rev. Lett.* **2015**, *114*, 170601.
- (11) Malolepsza, E.; Kim, J.; Keyes, T. *J. Phys.: Conf. Ser.* **2015**, *640*, 012003.
- (12) Kim, J.; Keyes, T.; Straub, J. E. *J. Chem. Phys.* **2011**, *135*, 161103.
- (13) Ferrenberg, A. M.; Swendsen, R. H. *Phys. Rev. Lett.* **1989**, *63*, 1195.
- (14) Gross, D. H. E.; Kenney, J. J. *J. Chem. Phys.* **2005**, *122*, 224111.
- (15) Schnabel, S.; Seaton, D.; Landau, D.; Bachmann, M. *Phys. Rev. E* **2011**, *84*, 011127.
- (16) Bachmann, M. *Thermodynamics and Statistical Mechanics of Macromolecular Systems*; Cambridge University Press: Cambridge, UK, 2014.
- (17) Stillinger, F. H.; Weber, T. A. *Phys. Rev. B: Condens. Matter Mater. Phys.* **1985**, *31*, 5262.
- (18) Molinero, V.; Moore, E. B. *J. Phys. Chem. B* **2009**, *113*, 4008.
- (19) Martyna, G. L.; Tobias, D. J.; Klein, M. L. *J. Chem. Phys.* **1994**, *101*, 4177.
- (20) Parrinello, M.; Rahman, A. *J. Appl. Phys.* **1981**, *52*, 7182.
- (21) Tuckerman, M. E.; Alejandre, J.; Lopez-Rendon, R.; Jochim, A. L.; Martyna, G. J. *J. Phys. A: Math. Gen.* **2006**, *39*, 5629.
- (22) Shinoda, W.; Shiga, M.; Mikami, M. *Phys. Rev. B: Condens. Matter Mater. Phys.* **2004**, *69*, 134103.
- (23) Steinhardt, P.; Nelson, D. R.; Ronchetti, M. *Phys. Rev. B: Condens. Matter Mater. Phys.* **1983**, *28*, 784.
- (24) Lechner, W.; Dellago, C. *J. Chem. Phys.* **2008**, *129*, 114707.
- (25) GitHub. <https://github.com/WolfgangLechner/StructureAnalysis>.
- (26) Li, T.; Donadio, D.; Russo, G.; Galli, G. *Phys. Chem. Chem. Phys.* **2011**, *13*, 19807–19813.
- (27) Moore, E. B.; de la Llave, E.; Welke, K.; Scherlis, D. A.; Molinero, V. *Phys. Chem. Chem. Phys.* **2010**, *12*, 4124–4134.
- (28) Binder, K.; Block, B.; Virnau, P. *Am. J. Phys.* **2012**, *80*, 1099.
- (29) MacDowell, L. G.; Virnau, P.; Müller, M.; Binder, K. *J. Chem. Phys.* **2004**, *120*, 5293.
- (30) Hardy, S. C. *Philos. Mag.* **1977**, *35*, 471–484.
- (31) Hilling, W. B. *J. Cryst. Growth* **1998**, *183*, 463–468.
- (32) Anderson, R.; Llamedo, M.; Tohidi, B.; Burgass, R. W. *J. Phys. Chem. B* **2003**, *107*, 3507.
- (33) Gránásy, L. *J. Mol. Struct.* **1999**, *485–486*, 523–536.
- (34) Huang, J.; Bartell, L. S. *J. Phys. Chem.* **1995**, *99*, 3924–3931.
- (35) Rozmanov, D.; Kuslik, P. G. *J. Chem. Phys.* **2012**, *137*, 094702.
- (36) Shultz, M. J.; Bisson, P. J.; Brumberg, A. *J. Phys. Chem. B* **2014**, *118*, 7972–7980.
- (37) Stillinger, F. H. *Science* **1995**, *267*, 1935.
- (38) Kim, J.; Keyes, T.; Straub, J. E. *Phys. Rev. E* **2009**, *79*, 030902.
- (39) Malkin, T. L.; Murray, B. J.; Brukhno, A. V.; Anwar, J.; Salzmann, C. G. *Proc. Natl. Acad. Sci. U. S. A.* **2012**, *109*, 1041–1045.
- (40) Malkin, T. L.; Murray, B. J.; Salzmann, C. G.; Molinero, V.; Pickering, S. J.; Whale, T. F. *Phys. Chem. Chem. Phys.* **2015**, *17*, 60–76.
- (41) Kuhs, W. F.; Bliss, D. V.; Finney, J. L. *J. Phys. Colloques* **1987**, *48*, C1–631–C1–636.
- (42) Carignano, M. A. *J. Phys. Chem. C* **2007**, *111*, 501–504.
- (43) Hansen, T. C.; Koza, M. M.; Kuhs, W. F. *J. Phys.: Condens. Matter* **2008**, *20*, 285104.
- (44) Pirzadeh, P.; Kuslik, P. G. *J. Am. Chem. Soc.* **2011**, *133*, 704–707.
- (45) Moore, E. B.; Molinero, V. *Phys. Chem. Chem. Phys.* **2011**, *13*, 20008–20016.
- (46) Kuhs, W. F.; Sippel, C.; Falenty, A.; Hansen, T. C. *Proc. Natl. Acad. Sci. U. S. A.* **2012**, *109*, 21259–21264.
- (47) Moore, E. B.; Allen, J. T.; Molinero, V. *J. Phys. Chem. C* **2012**, *116*, 7507–7514.
- (48) Quigley, D. *J. Chem. Phys.* **2014**, *141*, 121101.
- (49) Carr, T. H. G.; Shephard, J. J.; Salzmann, C. G. *J. Phys. Chem. Lett.* **2014**, *5*, 2469–2473.
- (50) Quigley, D. *J. Chem. Phys.* **2014**, *141*, 121101.
- (51) Tanaka, H. *J. Chem. Phys.* **1998**, *108*, 4889.